Nano Research

Open Access

Research Article

Wafer-scale growth of ultrathin amorphous tellurium oxide via pulsed laser deposition for p-channel transistors

Fu Huang[1,2,§], Yue Zheng[2,§] ✉, Lei Tang[3], Qiang Guo[2], Ming Huang[2], Ke Jiang[2], Runzhang Xu[4], Haizhe Zhong[2] ✉, and Cheng Han[2] ✉

[1] School of Environmental and Life Sciences, Nanning Normal University, Nanning 530100, China
[2] State Key Laboratory of Radio Frequency Heterogeneous Integration, and International Collaborative Laboratory of 2D Materials for Optoelectronics Science and Technology of Ministry of Education, Institute of Microscale Optoelectronics, Shenzhen University, Shenzhen 518060, China
[3] Songshan Lake Materials Laboratory, Dongguan 523808, China
[4] Department of Physics, The Hong Kong University of Science and Technology, Hong Kong, China
§ Fu Huang and Yue Zheng contributed equally to this work.

Cite this article: *Nano Research*, **2026**, *19*, 94909005. https://doi.org/10.26599/NR.2026.94909005

ABSTRACT: Oxide semiconductors are promising building blocks for complementary transparent electronics, and however p-type oxide semiconductors suffer from limited material choice and low carrier mobility as compared to their n-type counterparts. Herein, we demonstrate the wafer-scale growth of amorphous tellurium oxide (TeO_x) thin films with p-type transport characteristics, through a pulsed laser deposition (PLD) method coupled with a low-temperature post-annealing treatment. Ultrathin TeO_x with the thickness down to several nanometers is prepared by oxidizing the Te thin films precisely deposited and controlled by PLD technique, where their stoichiometric ratio can be modulated by the annealing time. Moreover, the optical bandgap of TeO_x is found to be varied from 0.59 to 0.98 eV during the oxidation process. As a result, the TeO_x-based field-effect transistors exhibit a competitive hole transport behavior as compared to reported amorphous TeO_x, along with the current on/off ratio exceeding 2×10^3 (1.3×10^7) and hole mobility of 47.6 ± 2 $cm^2 \cdot V^{-1} \cdot s^{-1}$ (41.8 ± 0.5 $cm^2 \cdot V^{-1} \cdot s^{-1}$) at 300 K (80 K). Our findings promise a facile and controllable approach to synthesize wafer-scale and ultrathin p-type oxides for future complementary electronics.

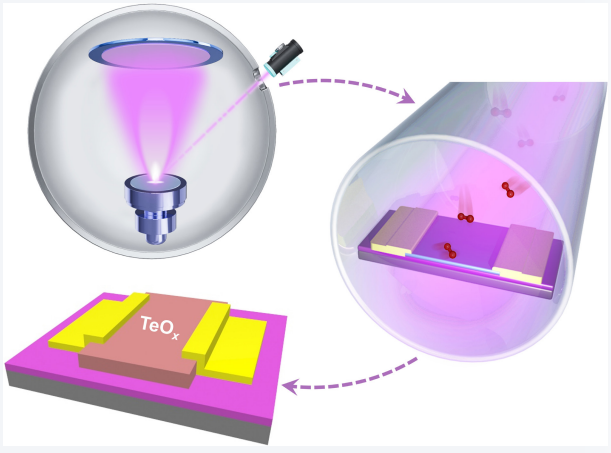

KEYWORDS: p-type oxide semiconductors, tellurium oxide, wafer-scale growth, tunable bandgap, field-effect transistors

1 Introduction

The family of oxide semiconductors offers a promising material platform for building up transparent or sensing electronic devices, including displays, integrated circuits, and chemical sensors [1–5]. Although n-type oxide semiconductors with high mobility have been widely explored (e.g., InGaZnO, SnO_2, ZnO) [6–9], the development of p-type counterparts is still limited by the narrow material choice and low hole mobility due to the strong carrier localization near valence band edge [10, 11], which is a major obstacle to achieve oxide-based complementary electronics [12–15]. Tellurium oxide (TeO_x), a high-mobility p-type semiconductor, has recently attracted intensive research attention for its tunable electronic band structures, compatibility with van der Waals (vdW) heterostructures, and potential for flexible electronics [16–22]. These attributes position TeO_x as one of the rare candidates capable of filling the performance gap left by conventional p-type oxides.

Over the past decades, a variety of techniques has been developed to synthesize TeO_x thin films, including physical vapor deposition (PVD) [23, 24], chemical bath deposition [25], sol–gel processing [26], and etc. [16, 27]. For example, TeO_x can be easily obtained from radio frequency sputtering of Te target in an Ar-O_2

Received: April 20, 2026; **Revised:** June 17, 2026
Accepted: July 7, 2026

✉Address correspondence to Yue Zheng, zhengyue@szu.edu.cn; Haizhe Zhong, haizhe.zhong@szu.edu.cn; Cheng Han, hancheng@szu.edu.cn

atmosphere or thermal evaporation of TeO_2 powder [24], which have been mainly used for optical storage or gas-sensing applications rather than field-effect transistors (FETs) because of their wide bandgap, high thickness (tens to hundreds of nanometers), and poor stoichiometric controllability. For oxide thin films used in FETs, even minor variation in stoichiometry (e.g., oxygen content) can remarkably impact on their band structures, defect states, and carrier density, thereby deteriorating device-to-device uniformity and reproducibility. A significant advance was made in 2021: Ali et al. reported a fancy scheme to grow ultrathin β-phase TeO_2 by rolling eutectic Te-Se droplets across the substrate with the help of a tip in the air, thus achieving p-type FETs with an on/off ratio of 10^6 and average mobility of 146 $cm^2 \cdot V^{-1} \cdot s^{-1}$ [16]. Nevertheless, this growth method relies on mechanical and delicate manipulation of droplets, which is potentially not applicable to the large-scale production and integration. Soon after that, Liu et al. proposed a modified evaporation strategy that deposited a mixed phase of tellurium/selenium within an amorphous tellurium suboxide matrix, enabling Se-alloyed TeO_x thin films with wafer-scale uniformity and long-term stability. Despite these improvements, the prepared films remain relatively thick (~ 15 nm), which limits their applications in short-channel transistors, and high-temperature (~ 225 °C) post-annealing is still required [27]. Very recently, a high-performance amorphous tellurium trioxide (a-TeO_3) was achieved by oxidizing the solution-grown two-dimensional (2D)-Te crystals via ozone treatment [19], presenting a hole mobility as high as 238.6 $cm^2 \cdot V^{-1} \cdot s^{-1}$. However, both thickness and area of a-TeO_3 are seriously limited by the solution-based growth method, giving the thick nanoflakes with the lateral size up to 100 μm. As a result, the development of a controllable synthetic method for the wafer-scale production of atomically thin TeO_x nanosheets remains a critical challenge.

In this work, we present the wafer-scale growth of ultrathin amorphous TeO_x films through the pulsed-laser deposition (PLD) of Te thin films combined with a low-temperature post-annealing process. The use of PLD technique enables the precise control of film thickness down to several nanometers by tuning laser pulses and provides the wafer-scale deposition of thin films with uniform composition and morphology. In addition, a post-annealing treatment at ~ 180 °C was implemented to oxidize as-deposited Te, which results in TeO_x thin films with the stoichiometry and optical bandgap controlled by the annealing time. The stoichiometric ratio and optical bandgap of TeO_x can be significantly increased from 0.34 to 1.49 and from 0.59 to 0.98 eV during the annealing process, as revealed by X-ray photoelectron spectroscopy (XPS) and ultraviolet–visible-near infrared (UV–Vis-NIR) absorption measurements. Finally, p-channel FETs were achieved on the as-grown TeO_x thin films, exhibiting a current on/off ratio of approximately 2×10^3 at 300 K and 1.3×10^7 at 80 K, together with the hole mobility of 47.6 ± 2 $cm^2 \cdot V^{-1} \cdot s^{-1}$ at 300 K and 41.8 ± 0.5 $cm^2 \cdot V^{-1} \cdot s^{-1}$ at 80 K. The device performance is comparable to the previously reported amorphous TeO_x thin films [16, 19, 21, 22, 27].

2 Result and discussion

PLD, a technique that allows near-stoichiometric transfer of target material to the substrate, was firstly employed to obtain high-quality ultrathin Te films in wafer scale [28, 29]. As illustrated in Fig. 1(a), a 248 nm KrF pulsed laser was focused onto a Te target positioned 30 cm below the SiO_2 substrate, and uniform Te films with different thickness were deposited by optimizing the laser pulse energy and adjusting the number of deposition cycles. Figure 1(b) shows an as-deposited continuous Te film uniformly covering a 4-inch SiO_2 substrate. These results demonstrate the excellent structural uniformity of the Te films over the wafer scale. The tunable thickness of Te films as a function of pulse number (150–300 cycles) was verified by atomic force microscopy (AFM) (Fig. 1(c) and Figs. S2(a)–S2(g) in the Electronic Supplementary Material (ESM)), which exhibits a linear dependence on the number of laser pulses (~ 0.02 nm·$pulse^{-1}$) (Fig. 1(d)) along with a low Ra roughness (Fig. S2(h) in the ESM). Furthermore, two characteristic vibration modes were observed in the Raman spectra (Fig. 1(e)), corresponding to the A_1 and E_2 modes of Te [30]. Notably, both the A_1 and E_2 modes exhibit a "red shift" of ~ 3.2 cm^{-1} (from 126.6 to 123.4 cm^{-1}) and ~ 2.3 cm^{-1} (from 144.1 to 141.8 cm^{-1}), respectively, as the film thickness increases (Fig. 1(f)). This behavior can be attributed to the unique helical-chain structure of Te and the weakened interlayer long-range Coulombic interactions in thicker films [31, 32]. Overall, these results demonstrate the excellent thickness controllability and homogenous surface of the as-prepared ultrathin Te films. To evaluate the wafer-scale uniformity of the as-deposited Te films, Raman measurements were performed over a 16 × 16 grid with 256 sampling points across the entire wafer (Fig. S3 in the ESM). Figure S4(a) in the ESM presents the overlaid Raman spectra collected from all measurement locations. The characteristic A_1 and E_2 Raman modes exhibit tiny spatial variation in peak position, intensity, and full width at half maximum (FWHM), as summarized in Figs. S4(b)–S4(d) in the ESM, which suggests the excellent structural uniformity for Te films.

Te-based back-gated FETs (Fig. 1(g)), with both the channel length and width fixed to 100 μm, were subsequently fabricated on Si/SiO_2 substrates (285 nm oxide thickness) by patterning Pd/Au source-drain electrodes to investigate their electrical properties. Figure 1(h) presents the thickness-dependent transfer characteristics of Te films with the thickness ranging from 2.9 to 6.1 nm. Except for the device based on the 2.9 nm, all other FETs exhibit p-dominant transport properties, which can be attributed to the relatively high valence-band edge of Te. In addition, a pronounced hysteresis behavior is observed, originating from native defects and charge trapping in Te films [33]. The effective hole mobility (μ) of the Te-based FETs was calculated using the following equation [16]

$$\mu = \frac{L}{WC_i V_{DS}} \cdot \frac{dI_{DS}}{dV_G} \quad (1)$$

where C_i is the gate capacitance per unit area (12.1 nF·cm^{-2} for 285 nm SiO_2) [34, 35], and L and W are the channel length and width, respectively. Notably, as the thickness of the Te thin film increased, the extracted hole mobility dramatically improved from 0.02 ± 0.02 to 102.8 ± 8 $cm^2 \cdot V^{-1} \cdot s^{-1}$(Fig. 1(i), red dotted line). This enhancement may be associated with the thickness-dependent bandgap narrowing in Te. Previous studies have shown that increasing Te thickness can facilitate hole injection and reduce contact resistance by thickness-modulated band engineering at the metal/Te interface [36]. As a result, the mobility extracted from thinner films is significantly underestimated, whereas thicker films more closely reflect the intrinsic channel mobility. In contrast, the current on/off ratio exhibits the opposite trend, which decreases significantly from ~ 3200 to ~ 50 (Fig. 1(i), blue dotted curve) with

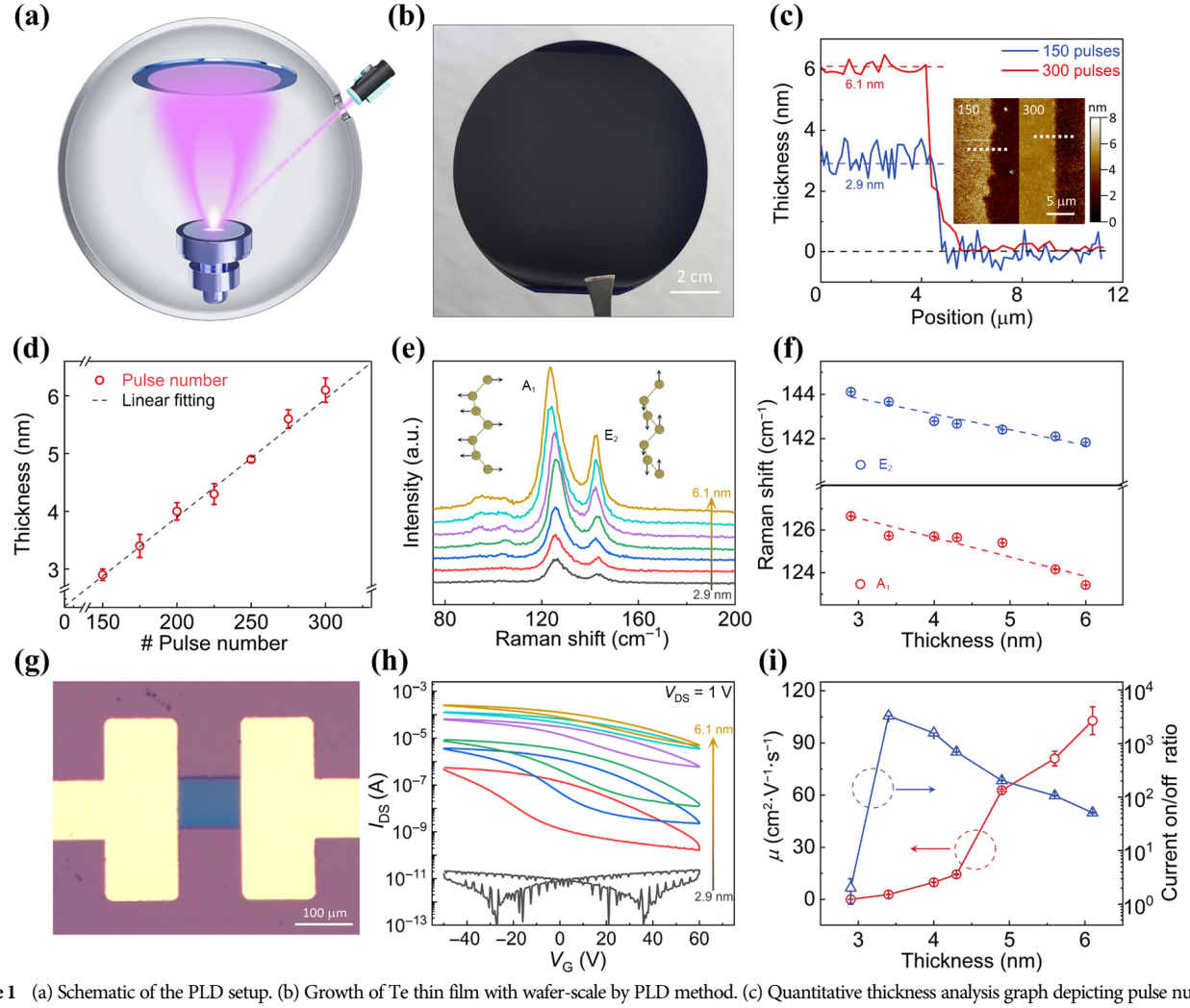

Figure 1 (a) Schematic of the PLD setup. (b) Growth of Te thin film with wafer-scale by PLD method. (c) Quantitative thickness analysis graph depicting pulse numbers of 150 (blue line, 2.9 nm) and 300 (red line, 6.1 nm) times from the insets of AFM topographic images. (d) The thickness of Te thin film depends on the pulse number of PLD. (e) Raman spectra for Te thin films with different thicknesses. (f) Detailed plots illustrating the variation in Raman positions of the A_1 and E_2 modes of Te as a function of thickness. (g) Optical image of a Te-based FET. (h) Transfer characteristics (V_{DS} = 1 V) of Te-based FETs as a function of thickness under dark and vacuum conditions. (i) Thickness-dependent mobilities and I_{on}/I_{off} ratios of Te-based FETs.

increasing film thickness, due to reduced electrostatic gate control in thicker channels [30, 37].

The 4.9 nm Te-based transistors (Fig. S5 in the ESM), which simultaneously exhibit high mobility and large current on/off ratio (Fig. 1(i)), were further oxidized to investigate the electrical properties of TeO_x-based FETs. The devices were placed at the center of a tubular furnace and annealed under an oxygen atmosphere with a flow rate of 200 sccm at 180 °C for varying durations ranging from 2 to 8 h (Fig. 2(a)). As illustrated in Fig. 2(b), the thickness of the measured film was slightly reduced to 4.5 nm after 8 h oxidization, indicating that the oxidation proceeds in a relatively mild manner [19]. To evaluate the wafer-scale uniformity of TeO_x thin films, optical microscopy (Fig. S6 in the ESM) and AFM (Fig. S7 in the ESM) measurements were conducted at 15 representative locations across the entire wafer. All inspected regions exhibit the uniform morphology without noticeable defects. The corresponding AFM images reveal the atomically smooth surface with the roughness (Ra) below 0.5 nm at all measured locations (Fig. S8 in the ESM), confirming the excellent morphological uniformity of TeO_x. Figure 2(c) exhibits the evolution of XRD pattern as a function of annealing time. The pristine Te exhibits clear diffraction peaks of (020), (111), and (133). Upon thermal oxidation, the intensity of these peaks progressively decreases with increasing annealing time. After prolonged oxidation of 8 h, these diffraction peaks nearly disappear, suggesting the loss of long-range crystalline order and the gradual transformation from crystalline Te to amorphous TeO_x.

Raman spectra were collected from the sample annealed for different duration. As shown in Fig. 2(d), a characteristic Raman peak near 618 cm^{-1} gradually appears and increases in intensity with increasing annealing time, which indicates the progressive oxidation of Te and the formation of amorphous TeO_x during thermal oxidation [19, 38]. The structural uniformity of as-grown TeO_x films was further investigated by wafer-scale Raman characterizations. Raman spectra were collected from the same 16 × 16 grid (256 points) after thermal oxidation. As shown in Fig. S9(a) in the ESM, all spectra exhibit a characteristic Raman peak near 618 cm^{-1}. The extracted peak position, intensity, and FWHM (Figs. S9(b)–S9(d) in the ESM) show small spatial variation across the wafer, which provides direct spectroscopic evidence for the wafer-scale uniformity of the TeO_x films. High-resolution transmission electron microscopy (HRTEM) measurements were performed to

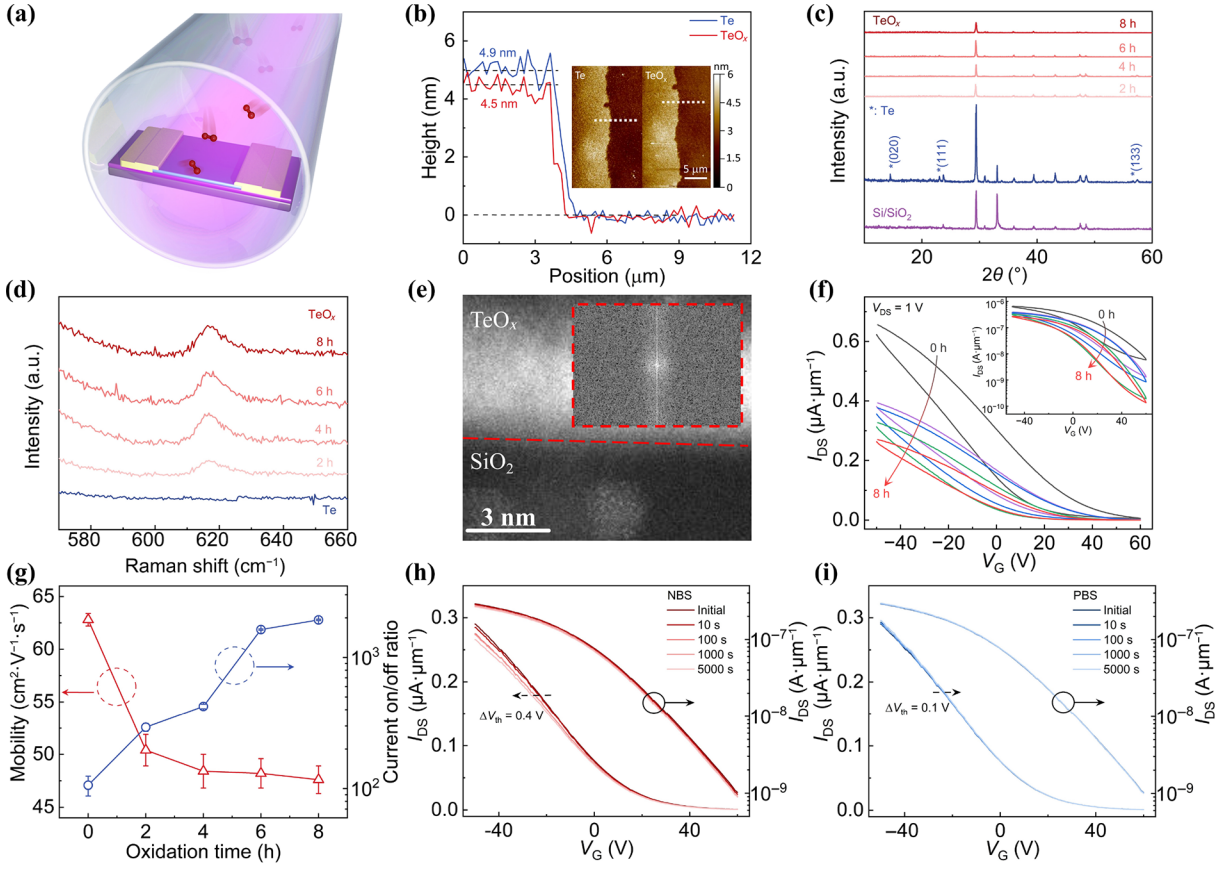

Figure 2 (a) Schematic of the oxidation reaction for the fabrication of TeO_x-based FETs. (b) The height profiles show the Te thickness (blue line, 4.9 nm) and TeO_x thickness (red line, 4.5 nm) from the insets of AFM topographic images. (c) XRD spectra of Te and TeO_x thin film as a function of annealing time. (d) Raman spectra of TeO_x thin films as a function of annealing time (0, 2, 4, 6, and 8 h). A characteristic Raman peak near 618 cm^{-1} gradually appears with increasing intensity. (e) HRTEM image and the corresponding FFT image. (f) Transfer characteristics (V_{DS} = 1 V, the inset showed in log scale) of TeO_x-based FETs as a function of annealing time under dark and vacuum conditions. (g) Annealing time-dependent mobilities and I_{on}/I_{off} ratios of TeO_x-based FETs. (h) and (i) Bias stability of TeO_x FETs. Transfer curves under (h) negative bias stress (NBS, −50 V) and (i) positive bias stress (PBS, +50 V).

directly reveal the crystal structure of TeO_x. As shown in Fig. 2(e), no distinguishable lattice fringes or nanocrystallites can be observed within the TeO_x layer. The corresponding FFT pattern exhibits a diffuse halo without diffraction spots or rings, confirming the absence of long-range crystallinity. Furthermore, energy-dispersive X-ray spectroscopy (EDS) elemental mappings demonstrate the homogeneous distribution of Te and O in the thin film (Fig. S10 in the ESM). The transfer characteristics of TeO_x thin films as a function of different annealing times are shown in Fig. 2(f) (the inset showed in log scale), revealing clear p-type transport properties. Moreover, the I_{DS}–V_{DS} output curves exhibit linear current–voltage behavior at a gate voltage of −50 V, confirming the formation of Ohmic contacts (Fig. S11 in the ESM) [37]. Figure 2(g) summarizes the evolution of the hole mobility and current on/off ratio as a function of oxidization time. With the annealing time prolonged from 0 to 8 h, the mobility decreases from 62.8 ± 0.6 to ~ 47.6 ± 2 $cm^2 \cdot V^{-1} \cdot s^{-1}$, attributed to increased carrier scattering during the crystalline-to-amorphous transition from Te to TeO_x [39]. In contrast, the on/off ratio increases from ~ 10^2 to over 10^3 due to the enhanced oxygen incorporation, which broadens the bandgap of films [39]. Negative bias stress (NBS) and positive bias stress (PBS) measurements were performed to evaluate the device stability, where the stress duration varied from 10 to 5000 s under a gate bias of −50 and +50 V, respectively. As shown in Figs. 2(h) and 2(i), the transfer characteristics exhibit a minor shift after prolonged gate-bias stressing (−0.4 V under NBS and +0.1 V under PBS after 5000 s). The excellent bias stability indicates a low density of charge trapping centers at the dielectric/channel interface and within the amorphous TeO_x layer [27]. The reproducibility of fabricated devices was further evaluated by batch-to-batch statistical analysis. Figure S12(a) in the ESM compares the transfer characteristics of FETs fabricated on separate wafers (two batches), which exhibit similar electrical performance. Statistical analysis reveals average field-effect mobilities of 47.6 ± 2.0 and 45.7 ± 1.8 $cm^2 \cdot V^{-1} \cdot s^{-1}$ for Batch 1 (12 devices) and Batch 2 (11 devices), respectively (Fig. S12(b) in the ESM). Although the corresponding $\log(I_{on}/I_{off})$ differs between two batches (3.31 ± 0.11 and 2.32 ± 0.10, Fig. S12(c) in the ESM), the small variation in both mobility and on-state current demonstrates good reproducibility of transport behavior in fabricated devices.

XPS measurements were performed to elucidate the oxidation degree and verify the oxygen atomic ratio of as a function of annealing time. As demonstrated in Fig. 3(a), the Te $3d_{5/2}$ components corresponding to Te–Te (Te^0), Te–O (Te^{2+}), and Te–O_2 (Te^{4+}) bonds appear at 572.7, 573.8, and 576.0 eV, respectively, while the Te $3d_{3/2}$ counterparts are located at 583.1, 584.0, and 586.4 eV [40–42]. For pristine Te without annealing, Te^0 is the dominated chemical state, where as Te^{2+} and Te^{4+} exhibit weak signals arising from the native oxidation of Te. When increasing the annealing time, the contributions from Te–Te and Te–O bonds

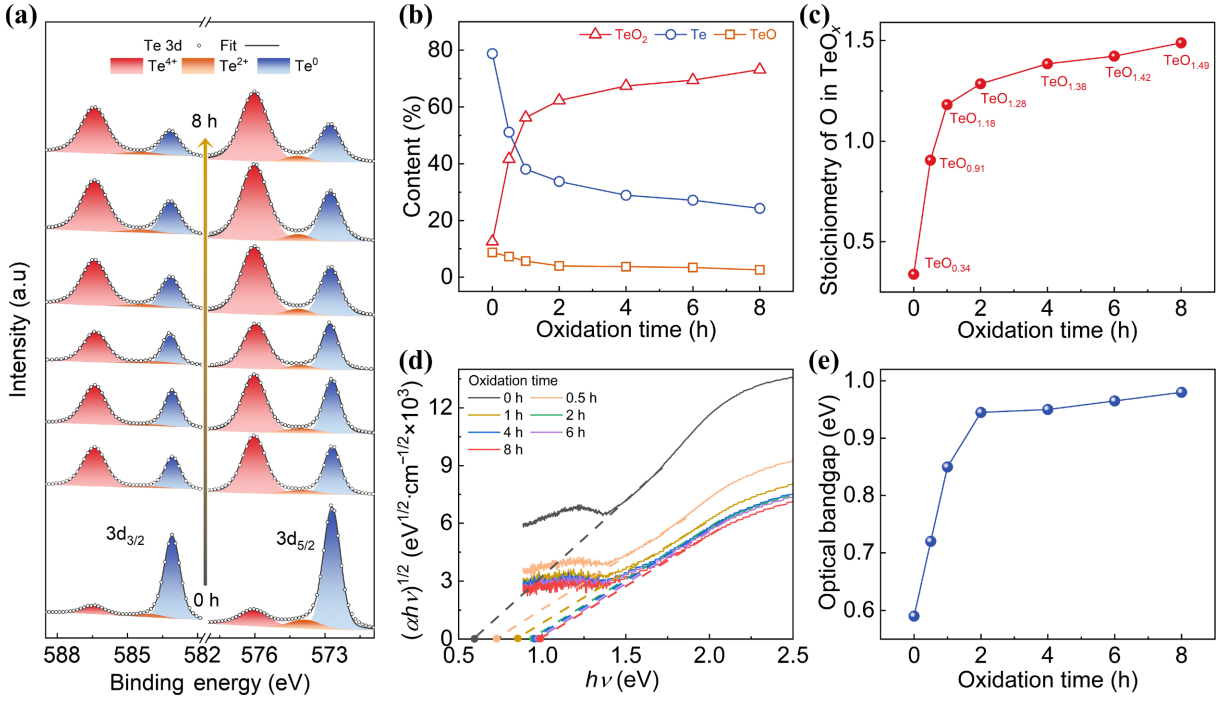

Figure 3 (a) XPS of Te 3d states in TeO_x thin film with different annealing time. (b) and (c) Depth profile of Te, TeO, and TeO_2 contents (b), and O/Te ratio in TeO_x thin films (c) by XPS measurement. (d) and (e) Optical bandgaps of TeO_x thin films with different annealing time extracted from the Cody plots of the absorption spectra.

progressively reduce, accompanied by a pronounced increase in the Te-O_2 components, indicating enhanced oxidation of Te. Meanwhile, the O 1s spectra show that the non-bridging oxygen (NBO) component dominates over the bridging oxygen (BO) component during the oxidation process. The lower binding energy of the NBO peak suggests an increased concentration of oxygen vacancies, which is associated with the formation of the amorphous oxide semiconductor (Fig. S13 in the ESM) [19]. Figure 3(b) illustrates the quantitative analysis of the Te, TeO, and TeO_2 components extracted from the corresponding peak areas, which exhibits a progressive increase in the TeO_2 fraction from 12.5% to 73.1% during oxidation. The exact value of x in TeO_x thin films was further calculated from the individual XPS peaks [40], which increases from 0.34 to 1.49 as the annealing time is extended from 0 to 8 h (Fig. 3(c)). These results reveal that the stoichiometric oxygen content in TeO_x can be well-controlled by varying the annealing time.

The optical bandgaps of TeO_x thin films with different stoichiometric ratios were further quantitatively extracted from UV–Vis-NIR absorption measurements (Fig. S14 in the ESM). Near the fundamental absorption edge, the relationship between the optical bandgap (E_g) and the absorption coefficient (α) can be described by

$$\alpha h\nu = B(h\nu - E_g)^{\eta} \quad (2)$$

where B is a characteristic parameter associated with the electronic transition, $h\nu$ is the photon energy, and η denotes the nature of the optical transition (η = 0.5 and η = 2 for direct and indirect semiconductors, respectively) [40, 43]. In addition, α can be calculated by

$$\alpha = 4\pi k/\lambda \quad (3)$$

where k is extinction coefficient, and λ is the optical wavelength. It is worth noting that TeO_x thin films with ~ 4.5 nm thickness are indirect bandgap semiconductors, therefore η is taken as 2 [44]. Figure 3(d) represents the Cody plots of $(\alpha\eta\nu)^{1/2}$ versus $h\nu$ for TeO_x thin films with different annealing time, where the extrapolated intercept at $(\alpha\eta\nu)^{1/2}$ = 0 corresponds to the optical bandgap. As summarized in Fig. 3(e), the extracted bandgap gradually increases from 0.59 eV at 0 h to 0.98 eV after 8 h of annealing. This monotonic bandgap broadening correlates well with the electrical and XPS results, which confirms that the annealing-driven increase of TeO_2 fraction and oxygen stoichiometry modifies the local bonding configuration, thereby governing the bandgap evolution in TeO_x thin films.

Oxide semiconductors are generally dominated by donor-like oxygen vacancies (such as V_o in IGZO or ZnO) [6, 8]. However, our XPS results reveal a high concentration of NBO species in TeO_x, which can introduce localized acceptor-like states near the valence band maximum (VBM), thus compensating donor-type oxygen vacancies. As a result, the Fermi level (E_F) shifts toward the valence band and facilitates the hole transport. To support this mechanism, UPS measurements were conducted on as-prepared TeO_x films. As shown in Fig. S15 in the ESM, the work function of TeO_x is extracted to ~ 4.6 eV, and its VBM is located at ~ 0.44 eV below E_F. Given the optical bandgap of ~ 0.98 eV for TeO_x, the VBM is estimated to be closer to Fermi level than conduction band minimum (CBM), consistent with its hole transport behavior. Furthermore, a clear trailing region (gray shaded area) can be observed between the VBM and E_F, corresponding to the NBO states. The proposed energy band diagram in Fig. S16 in the ESM illustrates that these localized NBO states exist between E_F and VBM (yellow shaded region), which act as active acceptor-like traps that dominate the hole transport. To investigate the electrical properties of TeO_x thin films, temperature-dependent transport measurements were performed on the 8 h-annealed $TeO_{1.49}$ devices to evaluate their potential for p-type FET applications. Figure 4(a)

and Fig. S17(a) in the ESM illustrate the transfer characteristics of $TeO_{1.49}$-based FETs measured under high vacuum over a temperature range from 80 to 300 K. At 300 K, the device exhibits an off-state current of 5.87×10^{-9} μA·μm^{-1} and a current on/off ratio of 2×10^3, which is in the same order of magnitude as that of other tellurium oxide transistors [19, 27, 45]. As the temperature decreases, the off-state current is progressively reduced, accompanied by a pronounced enhancement in the current on/off ratio. This pronounced temperature dependence indicates that the off-state conduction is dominated by thermally activated carriers rather than gate dielectric leakage. Such behavior is consistent with transport in narrow-bandgap amorphous semiconductors, where intrinsic carrier excitation and defect-assisted conduction can contribute to the residual current at elevated temperatures [37]. Consequently, the device performance is substantially improved at 80 K, yielding an ultralow off-state current of ~ 10^{-14} μA·μm^{-1} and a high current on/off ratio approaching 1.3×10^7. The transfer characteristics also exhibit a hysteretic behavior between forward and reverse gate voltage sweeps, similar to previous reports [19, 27, 45], indicating the presence of charge trapping processes in the device. Structural disorder and oxygen-vacancy-related defects in the amorphous TeO_x can introduce localized energy states within the bandgap, leading to the observed hysteresis [21]. To further evaluate the device stability, transfer characteristics were measured after 1, 7, and 14 days. As shown in Fig. S18 in the ESM, the devices exhibit minor degradation over time. Specifically, the threshold voltage shifts by ~ 0.99 V at 300 K and ~ 1.93 V at 80 K after 14 days, the small V_{th} shift (< 2 V over 14 days) indicates the stable device operation. Meanwhile, the on-state current shows a slight reduction, and the on/off ratio remains unchanged. These results indicate that the devices possess reasonable temporal stability, demonstrating their potential for reliable operation.

The hole mobility as a function of temperature is extracted in Fig. S17(b) in the ESM. A gradual increase in hole mobility is observed in the low temperature range (80–160 K), indicating that carrier transport is partially limited by trapping in localized states [46]. At higher temperatures (160–300 K), the mobility exhibits a weak temperature dependence following a power-law behavior of $\mu \propto T^{\gamma}$ with a small exponent $\gamma \sim 0.24$. Such weak temperature dependence suggests that carrier transport in TeO_x thin films is governed by thermally activated hopping or multiple trapping and release (MTR) processes through localized states rather than conventional band-like transport [47]. In this scenario, carriers repeatedly become trapped and released from defect states, forming percolation pathways for charge transport [48]. The presence of oxygen-vacancy-related defects, as revealed by XPS analysis, may contribute to the formation of these localized states and influence the overall transport behavior in amorphous TeO_x films [21].

The output characteristic curves measured at 80 and 300 K are shown in Figs. 4(b) and 4(c), respectively. The nearly linear I_{DS}–V_{DS} behavior in the negative gate voltage regime indicates Ohmic-like contacts between the metal electrodes and the TeO_x channel, suggesting efficient hole injection at the interface. To quantitatively evaluate the contact properties, Arrhenius plots extracted at different gate voltages are shown in Fig. S17(c) in the ESM [49]. The Schottky barrier height can be obtained from the equation [31]

$$= \frac{1000k_B}{q} S \quad (4)$$

where k_B is the Boltzmann constant, q is the elementary charge, and S is the slope of the Arrhenius plot. Figure S17(d) in the ESM summarizes the extracted Schottky barrier heights as a function of gate voltage, revealing an ultralow barrier of ~ 40 meV under flat-band condition. Transfer length method (TLM) measurements were also performed using devices with channel lengths ranging from 100 to 300 μm (Fig. S17(e) in the ESM) to extract the contact resistance. Linear fitting of the TLM data yields a contact resistance of approximately 37.8 kΩ·μm, confirming the favorable contact performance at the metal/TeO_x interface (Fig. S17(f) in the ESM).

The statistical distributions of device performance extracted from

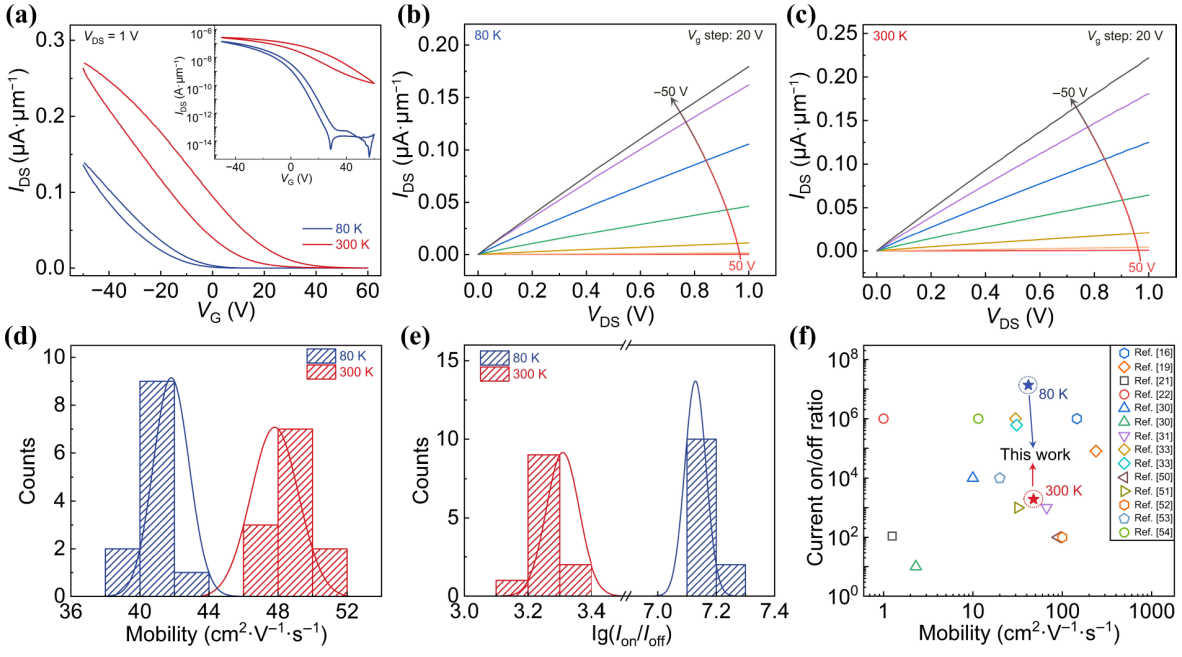

Figure 4 (a)–(c) Transfer (a) and output characteristics of $TeO_{1.49}$-based FET at 300 (b) and 80 K (c) under dark and vacuum conditions. (d) and (e) The statistical distribution of mobility (d) and lg(I_{on}/I_{off}) (e) for $TeO_{1.49}$-based FETs at 300 and 80 K conditions. (f) Comparison of carrier mobility and current on/off ratio of $TeO_{1.49}$-based FETs with the literatures.

tens of $TeO_{1.49}$ FETs measured at 80 and 300 K are shown in Figs. 4(d) and 4(e). Upon cooling from 300 to 80 K, the average hole mobility decreases from ~ 47.6 ± 2 to 41.8 ± 0.5 $cm^2 \cdot V^{-1} \cdot s^{-1}$, while the current on/off ratio improves by more than four orders of magnitude. Finally, the room-temperature field-effect mobility and current on/off ratio of previously reported Te-based and TeO_2-based FETs are summarized for comparison [16, 19, 21, 22, 30, 31, 33, 50–54]. As shown in Fig. 4(f) and Table S1 in the ESM, the TeO_x-based FETs in this work exhibit a competitive carrier mobility and current on/off ratio, especially under 80 K condition.

3 Conclusion

In summary, the wafer-scale growth of atomically thin amorphous TeO_x films has been achieved in a controlled manner by the oxidation of Te thin films prepared by PLD technique. By employing a low-temperature annealing process, both stoichiometry and optical bandgap of TeO_x can be effectively modulated by the annealing time, which varies from 0.34 to 1.49 and from 0.59 to 0.98 eV, respectively. As a result, TeO_x-based thin film transistors exhibit pronounced hole transport characteristics with a current on/off ratio exceeding 2×10^3 (1.3×10^7) and hole mobility of 47.6 ± 2 (41.8 ± 0.5 $cm^2 \cdot V^{-1} \cdot s^{-1}$) at 300 K (80 K), respectively. Our results provide a facile and controllable strategy for synthesizing wafer-scale and ultrathin TeO_x thin films, paving the way for their applications in integrated complementary electronics.

4 Methods

4.1 Fabrication of TeO_x thin film transistors

The fabrication process of TeO_x thin film transistor is shown in Fig. S1 in the ESM. Te thin films were deposited by PLD (Pioneer 180, Neocera) onto heavily doped p-type Si (p^{++}-Si) substrates with a 285 nm-thick SiO_2 layer. Prior to deposition, the substrates were sequentially cleaned in acetone, isopropanol, and DI water for 5 min each using an ultrasonic bath, followed by drying under nitrogen flow. A KrF excimer laser (Lambda-Physik LPX300, 248 nm) was focused onto the Te target with a spot size of 4 mm × 1 mm at a working distance of 30 cm. Te thin films were deposited through a shadow mask using different pulses number under the following conditions: laser energy of ~ 200 mJ, repetition rate of 1 Hz, chamber base pressure of ~ 10^{-8} torr, and room temperature. Subsequently, Pd/Au (20/100 nm) were deposited as source-drain (S/D) electrodes by thermal evaporation technique through a second shadow mask (W/L = 100 μm/100 μm). To fabricate a TeO_x transistor, the as-fabricated Te devices were annealed in the center of a homemade tubular furnace under an O_2 atmosphere with a flow rate of 200 sccm at 180 °C for various annealing durations.

4.2 Characterizations and electrical measurements

The thickness and surface morphology of Te thin films were characterized using AFM (Bruker, Dimension Icon). The Raman spectra were measured using a confocal Raman microscopy system (Witec Alpha 300) with a 532 nm excitation laser. XRD measurements were performed from an X-ray diffractometer (Rigaku, Ultima IV, Sevenoaks, UK) with Cu Kα radiation (λ = 1.5418 Å). UV–Vis-NIR absorption spectra were collected using a ScanPro Advance spectrophotometer. XPS and UPS measurements were carried out in an ESCA-lab system equipped with an Al Kα source (1486.6 eV). For HRTEM characterizations, cross-sectional HRTEM specimens of TeO_x were prepared by focused ion beam (FIB) milling and lift-out techniques. For electrical measurements, both Pd/Au electrodes and p^{++}-Si back gate were wire-bonded using Al wires. The electrical characteristics of the Te and TeO_x thin film transistors were measured using a Keithley 2600B Source measure unit (SMU).

Electronic Supplementary Material: Supplementary material (material characterization, device fabrication, and device performance of tellurium oxide) is available in the online version of this article at https://doi.org/10.26599/NR.2026.94909005.

Data availability

All data needed to support the conclusions in the paper are presented in the manuscript and the Electronic Supplementary Material. Additional data related to this paper may be requested from the corresponding author upon request.

Acknowledgements

Authors acknowledge the financial support from the National Natural Science Foundation of China (Nos. 12674522, 42467063, and 62404137), Shenzhen Science and Technology Program (Nos. JCYJ20250604182650067, JCYJ20240813142715021, JCYJ20220531103411026, JCYJ20241202124510014, and ZDSYS20170727101446 8), Shenzhen Strategic Emerging Industry Support Plan (No. F-2023-Z99-509043), Guangxi Natural Science Foundation (No. 2025JJA150150), College Young and Middle-aged Teachers' Basic Ability Improvement Project of Guangxi, China (No. 2024KY0402), and Guangxi Youth Talents Program. The authors thank Dr. Zhongyang Liu from the Photonics Center of Shenzhen University and Dr. Nan Jian from the Electron Microscope Center of Shenzhen University for their technique supports.

Declaration of competing interest

All the contributing authors report no conflict of interests in this work.

Author contribution statement

F. H., Y. Z., H. Z. Z., and C. H. conceived and designed the experiments. F. H. and Y. Z. performed the characterizations and device measurements. F. H., Y. Z., L. T., Q. G, M. H., K. J., R. Z. X., H. Z. Z., and C. H. analyzed the data. F. H., Y. Z., and C. H. wrote the manuscript. All authors discussed the results and commented on the manuscript.

Use of AI statement

None.

References

[1] Thomas, G. Invisible circuits. *Nature* **1997**, *389*, 907–908.
[2] Nomura, K.; Ohta, H.; Ueda, K.; Kamiya, T.; Hirano, M.; Hosono, H. Thin-film transistor fabricated in single-crystalline transparent oxide semiconductor. *Science* **2003**, *300*, 1269–1272.
[3] Wager, J. F. Transparent electronics. *Science* **2003**, *300*, 1245–1246.
[4] Yoo, S.; Kim, D. S.; Hong, W. K.; Yoo, J. I.; Huang, F.; Ko, H. C.; Park, J. H.; Yoon, J. Enhanced ultraviolet photoresponse

characteristics of indium gallium zinc oxide photo-thin-film transistors enabled by surface functionalization of biomaterials for real-time ultraviolet monitoring. *ACS Appl. Mater. Interfaces* **2021**, *13*, 47784–47792.

[5] Nomura, K.; Ohta, H.; Takagi, A.; Kamiya, T.; Hirano, M.; Hosono, H. Room-temperature fabrication of transparent flexible thin-film transistors using amorphous oxide semiconductors. *Nature* **2004**, *432*, 488–492.

[6] Huang, F.; Kim, S. Y.; Rao, Z. L.; Lee, S. J.; Yoon, J.; Park, J. H.; Hong, W. K. Protein biophotosensitizer-based IGZO photo-thin film transistors for monitoring harmful ultraviolet light. *ACS Appl. Bio Mater.* **2019**, *2*, 3030–3037.

[7] Huang, F.; Fang, F. E.; Zheng, Y.; You, Q.; Li, H. N.; Fang, S. F.; Cong, X. N.; Jiang, K.; Wang, Y.; Han, C. et al. Visible-light stimulated synaptic plasticity in amorphous indium-gallium-zinc oxide enabled by monocrystalline double perovskite for high-performance neuromorphic applications. *Nano Res.* **2023**, *16*, 1304–1312.

[8] Yoon, J.; Huang, F.; Shin, K. H.; Sohn, J. I.; Hong, W. K. Effects of applied voltages on the charge transport properties in a ZnO nanowire field effect transistor. *Materials* **2020**, *13*, 268.

[9] Atman, B.; Karakaş, G.; Uludağ, Y. Mathematical modeling of response dynamics of n-type SnO_2-based thick film gas sensor. *Mater. Sci. Semicond. Process.* **2025**, *190*, 109360.

[10] Hu, Y. Q.; Cho, K. Universal strain engineering for enhancing the hole mobility and dopability in p-type semiconductors. *J. Appl. Phys.* **2024**, *136*, 015701.

[11] Wang, Z. W.; Nayak, P. K.; Caraveo-Frescas, J. A.; Alshareef, H. N. Recent developments in p-type oxide semiconductor materials and devices. *Adv. Mater.* **2016**, *28*, 3831–3892.

[12] Sanal, K. C.; Vikas, L. S.; Jayaraj, M. K. Room temperature deposited transparent p-channel CuO thin film transistors. *Appl. Surf. Sci.* **2014**, *297*, 153–157.

[13] He, Q. Y.; Liu, Y.; Tan, C. L.; Zhai, W.; Nam, G. H.; Zhang, H. Quest for p-type two-dimensional semiconductors. *ACS Nano* **2019**, *13*, 12294–12300.

[14] Chhowalla, M.; Jena, D.; Zhang, H. Two-dimensional semiconductors for transistors. *Nat. Rev. Mater.* **2016**, *1*, 16052.

[15] Zhang, S. L.; Guo, S. Y.; Chen, Z. F.; Wang, Y. L.; Gao, H. J.; Gómez-Herrero, J.; Ares, P.; Zamora, F.; Zhu, Z.; Zeng, H. B. Recent progress in 2D group-VA semiconductors: From theory to experiment. *Chem. Soc. Rev.* **2018**, *47*, 982–1021.

[16] Zavabeti, A.; Aukarasereenont, P.; Tuohey, H.; Syed, N.; Jannat, A.; Elbourne, A.; Messalea, K. A.; Zhang, B. Y.; Murdoch, B. J.; Partridge, J. G. et al. High-mobility p-type semiconducting two-dimensional β-TeO_2. *Nat. Electron.* **2021**, *4*, 277–283.

[17] Guo, S. Y.; Zhu, Z.; Hu, X. M.; Zhou, W. H.; Song, X. F.; Zhang, S. L.; Zhang, K.; Zeng, H. B. Ultrathin tellurium dioxide: Emerging direct bandgap semiconductor with high-mobility transport anisotropy. *Nanoscale* **2018**, *10*, 8397–8403.

[18] Shen, Y. B.; Yan, X. X.; Zhao, S. K.; Chen, X. X.; Wei, D. Z.; Gao, S. L.; Han, C.; Meng, D. Ethanol sensing properties of TeO_2 thin films prepared by non-hydrolytic sol–gel process. *Sens. Actuators B: Chem.* **2016**, *230*, 667–672.

[19] Bang, S.; Lee, C.; Choi, D.; Park, D. Y.; Kim, D. H.; Lee, D.; Yi, D. J.; Song, J.; Yun, S. J.; Kim, D. W. et al. High performance p-channel transistor based on amorphous tellurium trioxide. *Adv. Mater.* **2025**, *37*, 2504948.

[20] Wang, J. C.; Zheng, H. C.; Kong, B.; Xu, X.; Feng, Z. Z.; Zeng, T. X.; Wang, W. T. Hybrid density functional study on the p-type conductivity mechanism in intrinsic point defects and group V element-doped 2D β-TeO_2. *ACS Appl. Mater. Interfaces* **2024**, *16*, 58545–58555.

[21] Yang, X. M.; Lee, J.; Le, Z. K.; He, M. F.; Zhu, H. H.; Wang, M. Y.; Xu, M. S.; Noh, Y. Y.; Liu, A. Quantifying and overcoming defect limitations in high-mobility amorphous p-type tellurium oxide transistors. *Adv. Funct. Mater.* **2026**, *36*, e18364.

[22] Wang, M. Y.; Zou, T. Y.; Reo, Y.; Kim, Y. S.; Kim, M. G.; Choi, M.; Park, Y.; Yang, K.; Kang, Y.; Zhu, H. H. et al. Sulfur redox mediator for low-temperature flexible amorphous oxide CMOS electronics. *Sci. Adv.* **2025**, *11*, eadz6914.

[23] Siciliano, T.; Di Giulio, M.; Tepore, M.; Filippo, E.; Micocci, G.; Tepore, A. Ammonia sensitivity of RF sputtered tellurium oxide thin films. *Sens. Actuators B: Chem.* **2009**, *138*, 550–555.

[24] Dewan, N.; Gupta, V.; Sreenivas, K.; Katiyar, R. S. Growth of amorphous TeO_x ($2 \le x \le 3$) thin film by radio frequency sputtering. *J. Appl. Phys.* **2007**, *101*, 084910.

[25] Kong, H.; Yeo, J. B.; Lee, H. Y. A study on the properties of tellurium-oxide thin films based on the variable sputtering gas ratio. *J. Korean Phys. Soc.* **2015**, *66*, 1744–1749.

[26] Hodgson, S. N. B.; Weng, L. Sol–gel processing of tellurium oxide and suboxide thin films with potential for optical data storage application. *J. Sol-Gel Sci. Technol* **2000**, *18*, 145–158.

[27] Liu, A.; Kim, Y. S.; Kim, M. G.; Reo, Y.; Zou, T. Y.; Choi, T.; Bai, S.; Zhu, H. H.; Noh, Y. Y. Selenium-alloyed tellurium oxide for amorphous p-channel transistors. *Nature* **2024**, *629*, 798–802.

[28] Apte, A.; Bianco, E.; Krishnamoorthy, A.; Yazdi, S.; Rao, R.; Glavin, N.; Kumazoe, H.; Varshney, V.; Roy, A.; Shimojo, F. Polytypism in ultrathin tellurium. *2D Mater.* **2019**, *6*, 015013.

[29] Reyes-Verdugo, L. A.; Gutiérrez-Lazos, C. D.; Santos-Cruz, J.; Chávez-Chávez, A.; Quiñones-Galván, J. G. Bi_2Te_3 thin films deposited by the combination of Bi and Te plasmas in a PLD process. *Micromachines* **2023**, *14*, 590.

[30] Wang, Y. X.; Qiu, G.; Wang, R. X.; Huang, S. Y.; Wang, Q. X.; Liu, Y. Y.; Du, Y. C.; Goddard, W. A.; Kim, M. J.; Xu, X. F. et al. Field-effect transistors made from solution-grown two-dimensional tellurene. *Nat. Electron.* **2018**, *1*, 228–236.

[31] Zhang, X.; Jiang, J. Z.; Suleiman, A. A.; Jin, B.; Hu, X. Z.; Zhou, X.; Zhai, T. Y. Hydrogen-assisted growth of ultrathin Te flakes with giant gate-dependent photoresponse. *Adv. Funct. Mater.* **2019**, *29*, 1906585.

[32] Yao, J. R.; Chen, F. F.; Li, J. J.; Du, J. L.; Wu, D.; Tian, Y. T.; Zhang, C.; Yang, J. K.; Li, X. J.; Lin, P. A high-performance short-wave infrared phototransistor based on a 2D tellurium/MoS_2 van der Waals heterojunction. *J. Mater. Chem. C* **2021**, *9*, 13123–13131.

[33] Zhao, C. S.; Batiz, H.; Yasar, B.; Kim, H.; Ji, W. B.; Scott, M. C.; Chrzan, D. C.; Javey, A. Tellurium single-crystal arrays by low-temperature evaporation and crystallization. *Adv. Mater.* **2021**, *33*, 2100860.

[34] Zhang, M. Y.; Liang, N. W.; Hao, D.; Chen, Z. X.; Zhang, F.; Yin, J.; Yang, Y. H.; Yang, L. S. Recent advances of SiO_x-based anodes for sustainable lithium-ion batteries. *Nano Res. Energy* **2023**, *2*, e9120077.

[35] Cao, W.; Bu, H. M.; Vinet, M.; Cao, M.; Takagi, S.; Hwang, S.; Ghani, T.; Banerjee, K. The future transistors. *Nature* **2023**, *620*, 501–515.

[36] Kim, M.; Ban, J.; Shin, U.; Lee, G.; Jun, J. H.; Lee, H. W.; Lee, B. H. Thickness-modulated band engineering for low-resistance contacts in ultrathin tellurium transistors. *ACS Nano* **2026**, *20*, 10358–10367.

[37] Amani, M.; Tan, C. L.; Zhang, G.; Zhao, C. S.; Bullock, J.; Song, X. H.; Kim, H.; Shrestha, V. R.; Gao, Y.; Crozier, K. B. et al. Solution-synthesized high-mobility tellurium nanoflakes for short-wave infrared photodetectors. *ACS Nano* **2018**, *12*, 7253–7263.

[38] Altaf, S.; Ijaz, H.; Haider, J.; Naz, M.; Aqeel, M.; Ul-Hamid, A.; Ikram, M.; Zulfiqar, S.; Ditta, S. A.; Shahbaz, A. et al. Influence of various transition metals incorporated into tellurium used as antimicrobial agent and textile dye degrader. *Appl. Nanosci.* **2020**, *10*, 4241–4254.

[39] Tan, C. L.; Amani, M.; Zhao, C. S.; Hettick, M.; Song, X. H.; Lien, D. H.; Li, H.; Yeh, M.; Shrestha, V. R.; Crozier, K. B. et al. Evaporated Se_xTe_{1-x} thin films with tunable bandgaps for short-wave infrared photodetectors. *Adv. Mater.* **2020**, *32*, 2001329.

[40] Wei, T.; Wei, J. S.; Zhang, K.; Zhang, L. Image lithography in telluride suboxide thin film through controlling "virtual" bandgap. *Photonics Res.* **2017**, *5*, 22–26.

[41] Zhou, L. Q.; Chen, C.; Jia, H. F.; Ling, C.; Banerjee, D.; Phillips, J. D.; Wang, Y. Q. Oxygen incorporation in ZnTeO alloys via molecular beam epitaxy. *J. Electron. Mater.* **2014**, *43*, 889–893.

[42] Huang, J. H.; Hsu, H. H.; Wang, D.; Lin, W. T.; Cheng, C. C.; Lee, Y. J.; Hou, T. H. Polymorphism control of layered $MoTe_2$ through two-dimensional solid-phase crystallization. *Sci. Rep.* **2019**, *9*, 8810.

[43] Shaaban, E. R. Optical constants and fitted transmittance spectra of varies thickness of polycrystalline ZnSe thin films in terms of spectroscopic ellipsometry. *J. Alloys Compd.* **2013**, *563*, 274–279.

[44] Wu, B. Z.; Liu, X. H.; Yin, J. R.; Lee, H. Bulk β-Te to few layered β-tellurenes: Indirect to direct band-Gap transitions showing semiconducting property. *Mater. Res. Express* **2017**, *4*, 095902.

[45] Huang, W. D.; Huang, B. B.; Bi, J. J.; Chen, J. Z.; Chen, Y. F.; Yang, J. J.; Zhong, J.; Liu, P.; Gao, Q. G. Enhanced mobility and stability in evaporated p-type TeO_x/Te transistors via UV-O_3-treated substrates. *Appl. Surf. Sci.* **2026**, *730*, 166367.

[46] Luo, Y. Z.; Flewitt, A. J. Revisiting multiple trapping and release charge transport in amorphous semiconductors exemplified by hydrogenated amorphous silicon. *J. Non-Cryst. Solids* **2025**, *654*, 123436.

[47] Huzaibi, H. U.; Han, S. T.; Zhang, M. Model representation in amorphous metal oxide thin-film transistors: A critical review. *npj Flex. Electron.* **2025**, *10*, 13.

[48] Wang, X.; Dodabalapur, A. Carrier velocity in amorphous metal-oxide-semiconductor transistors. *IEEE Trans. Electron Devices* **2021**, *68*, 125–131.

[49] Ye, J. F.; Liao, K.; Ge, X.; Wang, Z.; Wang, Y.; Peng, M.; He, T.; Wu, P. S.; Wang, H. L.; Chen, Y. F. et al. Narrowing bandgap of HfS_2 by Te substitution for short-wavelength infrared photodetection. *Adv. Opt. Mater.* **2021**, *9*, 2002248.

[50] Kim, T.; Choi, C. H.; Byeon, P.; Lee, M.; Song, A.; Chung, K. B.; Han, S.; Chung, S. Y.; Park, K. S.; Jeong, J. K. Growth of high-quality semiconducting tellurium films for high-performance p-channel field-effect transistors with wafer-scale uniformity. *npj 2D Mater. Appl.* **2022**, *6*, 4.

[51] Jiang, W.; Wang, X. D.; Chen, Y.; Wu, S. Q.; Wu, B. M.; Yang, X.; Lin, T.; Shen, H.; Meng, X. J.; Wu, X. et al. End-bonded contacts of tellurium transistors. *ACS Appl. Mater. Interfaces* **2021**, *13*, 7766–7772.

[52] Zhao, C. S.; Tan, C. L.; Lien, D. H.; Song, X. H.; Amani, M.; Hettick, M.; Nyein, H. Y. Y.; Yuan, Z.; Li, L.; Scott, M. C. et al. Evaporated tellurium thin films for p-type field-effect transistors and circuits. *Nat. Nanotechnol.* **2020**, *15*, 53–58.

[53] Cao, R.; Zhang, Y.; Wang, H. D.; Zeng, Y. H.; Zhao, J. L.; Zhang, L. Y.; Li, J. Q.; Meng, F. X.; Shi, Z.; Fan, D. Y. et al. Solar-blind deep-ultraviolet photodetectors based on solution-synthesized quasi-2D Te nanosheets. *Nanophotonics* **2020**, *9*, 2459–2466.

[54] Tan, P. K.; Niu, C.; Lin, Z. H.; Lin, J. Y.; Long, L. J.; Zhang, Y. Z.; Wilk, G.; Wang, H. Y.; Ye, P. D. Wafer-scale atomic layer-deposited TeO_x/Te heterostructure p-type thin-film transistors. *Nano Lett.* **2024**, *24*, 12433–12441.